Mitigating space charge in time-resolved photoelectron spectroscopy to study laser-heated copper dynamics in the high fluence regime

Anna Lévy ⬤,[*] Manuel De Anda Villa, Mohamed Hatifi, Emily Lamour ⬤, Stéphane Macé, Christophe Prigent,
Sébastien Steydli, Martino Trassinelli ⬤, and Dominique Vernhet
Institut des Nanosciences de Paris, Sorbonne Université, Campus Pierre et Marie Curie, CNRS UMR7588, 75005 Paris, France

Robert E. Grisenti[†]
GSI Helmholtzzentrum für Schwerionenforschung, 64291 Darmstadt, Germany

Ryszard Sobierajski ⬤ and Andrzej Wawro ⬤
Institute of Physics of the Polish Academy of Sciences, PL-02-668 Warsaw, Poland

Ludovic Lecherbourg ⬤[‡]
CEA, DAM, DIF, Arpajon 91297, France

Hervé Jouin ⬤, Rodrigue Bouillaud, Dominique Descamps, Fabien Dorchies ⬤, Nikita Fedorov,
Stéphane Petit ⬤, and Jérôme Gaudin ⬤
CNRS, CEA, CELIA (Centre Lasers Intenses et Applications), University of Bordeaux, UMR5107, F-33405 Talence, France

The performance of time-resolved photoelectron spectroscopy for the study of subpicosecond dynamics of laser-heated solids is often limited by space charge effects. The consequent shift and distortion of the photoelectron spectrum induced by electrons emitted by the ultrashort pump pulse is studied here using a fully coherent approach based on experimental measurements and space charge calculations. The temporal dynamics of the valence band of a copper sample is recorded before and after an 800 nm laser pump excitation at a fluence of 750 mJ/cm^2. The probe pulse is produced using a laboratory-based high-harmonics source delivering 25 fs pulses up to 100 eV photon energy. We extract the laser-heating contribution by comparing these measurements with space charge calculations based on particle-in-cell simulations of the pump and probe electron clouds mutual interaction on their way to the detector. The deduced picosecond dynamics associated to the electronic density of states shift is attributed to lattice changes with the help of hydrodynamic simulations including the two-temperature model.

I. INTRODUCTION

Photodriven processes have been proved, specially with the advent of ps-fs optical or free electron lasers, to be a fruitful playground to explore a huge variety of physical and chemical phenomena [1]. The energy of light, initially absorbed by the electronic system, drives matter to an out of equilibrium state. Subsequently, it relaxes via different channels facilitated by the interplay of charge, lattice, spin, and/or orbital degrees of freedom. Disentangling the different contributions and dynamics of these degrees of freedom requires experimental methods with temporal resolution shorter than the explored phenomenon, i.e., usually sub-picosecond. The

typical experimental scheme is the pump-probe configuration, where a pump pulse triggers the dynamical process while a delayed pulse probes the transient states of the sample. Several x-ray-based techniques are pertinent for time-resolved experiments [2] exploring relaxation processes. Each of them provides access to different observables, from atomic to electronic structures. Among those techniques, x-ray photoelectron spectroscopy is a measure of the occupied electronic density of states, but it goes well beyond when coupled with *ab initio* simulations, informing on the different degrees of freedom aforementioned [3–5].

In solids, while numerous experiments can be performed at low excitation density, i.e., at limited pump fluence, some processes require to excite a large fraction of the valence band electrons. In this case, photoelectron spectroscopy diagnostic can be limited by an intricate situation where electrons are photoemitted both by pump and probe pulses [6–10]. All these photoelectrons come into play and the physics that can be explored is drastically circumscribed by their mutual Coulomb interaction, leading to a dramatic distortion of the measured

---

[*]levy@insp.jussieu.fr
[†]Also at Institut für Kernphysik, Universität Frankfurt, 60486 Frankfurt am Main, Germany.
[‡]Also at Université Paris-Saclay, CEA, LMCE, Bruyères-le-Châtel 91680, France.
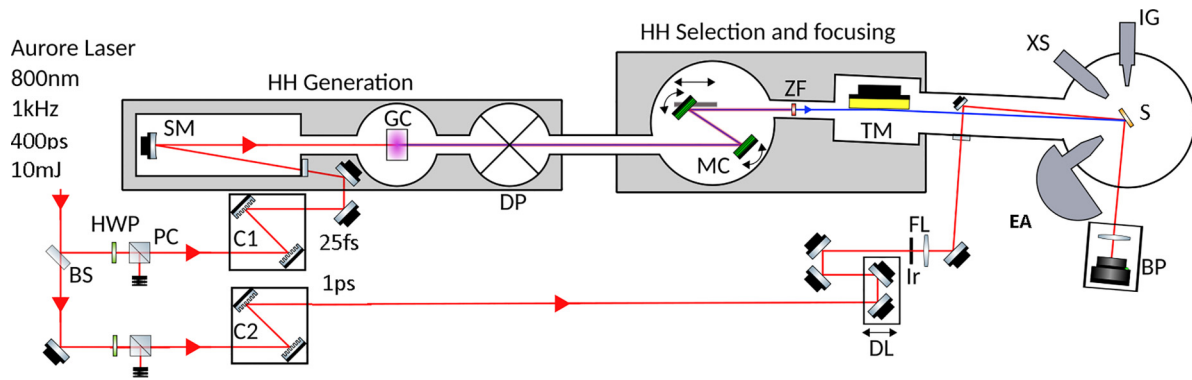
FIG. 1. Tr-PES experimental setup [BS: beam splitter; HWP: half-wave plate; PC: polarizing cube; C1(2): probe (pump) compressor; SM: spherical mirror; DL: delay line; Ir: 5 mm diameter iris; FL: focusing lens ($f = 2$ m); GC: gas cell filled with neon; DP: differential pumping; ZF: zirconium filter; MC: nondispersive XUV monochromator; TM: toroidal mirror; EA: electron energy analyzer; S: sample; XS: twin anode x-ray source; IG: ion gun for Ar^+ sputtering; BP: beam profiler].

photoemission spectrum. This so-called pump-induced space charge effect is hardly preventable and hence appeals for studies in order to evaluate the potential use of time-resolved x-ray photoemission spectroscopy in this regime of high pump fluence. Different works have been published on this topic exploring instrumental [6] or theoretical [7,8,11] approaches attempting either to reduce or to predict the space-charge-induced effects.

In this contribution, we address this question in a dedicated experimental investigation where ultrafast heating of a prototypical transition metal, copper, is triggered by a ps optical pump pulse. The pump fluence is adjusted to approach the solid-to-liquid phase transition, a typical situation where the pump pulse itself is able to trigger significant photoelectron emission. The dynamics of the copper valence band is probed by a fs x-ray pulse produced by high-order harmonic generation. We first briefly depict the experimental apparatus and then describe the experimental results. In order to interpret these results and disentangle space-charge from pump-heating induced effects, a multistep simulation procedure has been performed. The initial spectrum photoemitted by the pump pulse is modeled using the jellium-Volkov approximation [12–14]. These spectra are then used as input data for ASTRA [15], a particle-in-cell (PIC) simulation code that also includes the probe photoemitted electrons. The simulation results are then compared to the experimental ones in order to retrieve the copper valence band temporal evolution after the pump excitation. Finally, the deduced dynamics is discussed in relation to results obtained from hydrodynamic simulations using the ESTHER code [16].

II. EXPERIMENTAL DESCRIPTION

The experiment has been performed at the CELIA laboratory (CEntre Lasers Intenses et Applications, Bordeaux, France) on the Aurore platform described in detail in [17]. The Aurore laser facility (1 kHz, 800 nm, 25 fs, <7 mJ) supplies the experimental setup schematized in Fig. 1 associated with the Aurore beamline 3 dedicated to time-resolved photoemission spectroscopy (Tr-PES) on solids. In brief, the chirped laser pulse is divided into two parts in order to operate both the pump near-IR and the probe soft x-ray branches. Each beam

is independent in terms of pulse duration and energy thanks to their respective compressor (C1 and C2) and energy beam attenuator (half-wave plate and polarization cube).

The 800 nm pump beam is focused on the sample surface at an incidence angle of $43°$ with respect to the sample normal. The sample is positioned in the focal plane of an $f = 2$ m planoconvex lens preceded by a 5 mm diameter iris. The resulting focal spot pump diameter of 280×201 μm² FWHM (full width at half maximum) measured with an imaging system in the specular direction is kept constant for all measurements. The ellipsoidal shape results from the off-normal incidence angle. Using these focusing parameters, the incident pump laser fluence is varied in the range of 600 to 820 mJ/cm² by adjusting the energy in the pump beam. The pump pulse is stretched up to 1 ps FWHM pulse duration and is set in *s* polarization. Such a configuration was selected on the basis of preliminary experiments and results reported in literature [18], which show that, in these conditions, the space-charge effect is reduced.

The soft x-ray probe beam is produced by high-order harmonic generation (HHG) of the 25 fs, 800 nm laser pulse focused in a variable-length gas cell using a spherical mirror of 1 m focal length. The resulting comblike HHG spectrum is optimized in the photon energy range of 80 to 100 eV using neon gas as the generating medium. A single harmonic is then selected using a pair of multilayer mirrors (OptiX fab GmbH, Jena, Germany) optimized for this photon energy range, which preserves the nominal ultrashort pulse duration. The residual near-IR radiation is filtered out using a 110 nm thick Zr film (Luxel Corp.). The measurements presented here have been made using 88.4 eV (HHG 57) photons. The probe beam is then focused onto the sample surface using a 1 m focal length, grazing incidence, gold-coated toroidal mirror at an angle of $45°$ with respect to the sample normal. Its size is minimized as much as possible in order to probe a relatively homogeneous heated area of the sample surface. The resulting focal spot diameter is estimated around 185×124 μm² (FWHM) according to the measured size of the residual near-IR beam impinging on the sample surface. This value corresponds to an upper limit, as the x-ray beam intensity is proportional to a power law of the near-IR intensity: $I_X \propto I_{IR}^q$, where $q = 4$ from Ref. [19] measurements performed in Ar. A detailed
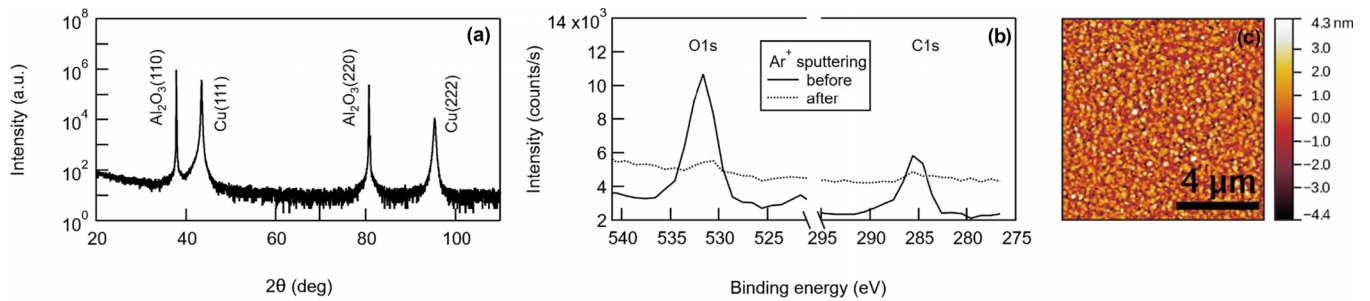
FIG. 2. Cu (48 nm)/V (2.5 nm)/Al$_2$O$_3$ (0.5 mm) sample characterization: (a) XRD, (b) XPS before and after Ar$^+$ sputtering measurements, and (c) AFM.

description of this specific soft x-ray beamline is reported in Ref. [17].

Both arms are recombined on the sample surface adjusting their spatial and temporal overlaps using the specular imaging system. The former is achieved by imaging the 800 nm focal spots of both optical paths. Their temporal synchronization is optimized by the appearance of the resultant interference pattern (as the IR pulse used to generate the HHG is synchronized with the soft x-ray pulse) using the motorized delay line installed on the pump branch. In the following, negative delays refer to a sample probing before pump irradiation.

This setup is used to probe the relaxation dynamics of a solid Cu sample heated by an ultrashort laser pulse using time-resolved photoelectron spectroscopy (Tr-PES) in the soft x-ray range. This is achieved in a dedicated ultrahigh vacuum chamber (UHV) at a pressure $< 1 \times 10^{-9}$ mbar. Details on the sample characterization and Tr-PES measurements are reported in the following subsections.

A. Sample characterization and preparation

According to previous measurements presented in Ref. [18], the sample roughness was carefully controlled and minimized for the purpose of this experiment in order to reduce the pump-induced electron emission and the resulting space charge effect. The 48 nm thick Cu sample has been therefore produced by molecular beam epitaxy (MBE) on a 0.5 mm thick sapphire substrate at the Institute of Physics of the Polish Academy of Sciences (Warsaw, Poland). The Cu and Al$_2$O$_3$ adherence is insured by a 2.5 nm vanadium interlayer.

A detailed characterization of the sample morphology has been performed using x-ray diffraction (XRD), x-ray reflectometry (XRR), and atomic force microscopy (AFM) diagnostics. According to these measurements of the as-grown sample summarized in Figs. 2(a) and 2(c), (111) surface crystallographic orientation, 1.4 nm rms (root mean square) sample roughness, and 2.1 nm superficial oxidation have been determined.

In addition, after introduction into the UHV interaction chamber, the sample has been submitted to 5 min of 600 eV Ar$^+$ sputtering adjusted to minimize surface contamination. The latter is monitored using Al K_α radiation of a twin anode x-ray source (RS40B1, Prevac) recording the C 1s and O 1s XPS (x-ray photoelectron spectroscopy) core levels before and after ion bombardment [see Fig. 2(b)]. The residual signal

observed after applying this cleaning procedure is most probably associated with the sample holder since no improvement has been observed by increasing the sputtering time. Sample annealing has not been applied in order to preserve the Cu thin layer which could be partly damaged by such a heating procedure. Finally, the morphological characterizations (AFM, XRD, XRR) have been performed before this sample preparation, which could affect the sample roughness. The above mentioned values can therefore be considered as lower limits for the laser-irradiated sample.

B. Time-resolved photoelectron spectroscopy measurements

The photoelectron spectra have been recorded using an electron energy analyzer (Thermo VG Scientific Clam IV) with a 9-channeltron detection head positioned in the sample's normal direction. Each spectrum is the result of the integration over 10 scans in order to average over the laser energy ($\simeq 1.1\%$ rms) and pointing fluctuations ($\simeq 3.6$ μrad rms) [17]. This acquisition time is selected to keep the measurement of a full pump/probe set at a given fluence sufficiently short to be recorded in a single day. The pass energy is set to 20 eV in order to optimize the instrumental spectral resolution ($\simeq 1$ eV FWHM). The dwell time is 200 ms with an energy step of 0.1 eV. The PES spectrum is recorded in the range of 81 to 91 eV electron kinetic energies where the Cu valence (3d) and conduction (4s) bands are expected [see Fig. 3(d) in black dotted line]. The smooth shape of the whole spectrum and, especially of, the Fermi level can be explained by the limited spectral resolution resulting from the analyzer parameters and HHG bandwidth ($\simeq 1.2$ eV). In the following, for sake of clarity, the PES spectrum will be referred to the Cu valence band.

For technical reasons associated with UHV conditions, the sample is refreshed only at the beginning of each pump/probe set of measurement, i.e., all delays for one given pump fluence. The PES spectrum of the pristine sample, with no pump irradiation, is therefore recorded before and after each run in order to characterize the Cu cold valence band and confirm that the sample has not undergone any irreversible modification after the interaction with the laser pump at 1 kHz. It is important to mention here that, for these reasons also, the investigated laser fluences and hence laser intensities are kept below the sample ablation threshold, which would make impossible any measurement in these conditions due to irreversible sample alteration at 1 kHz repetition rate. In these
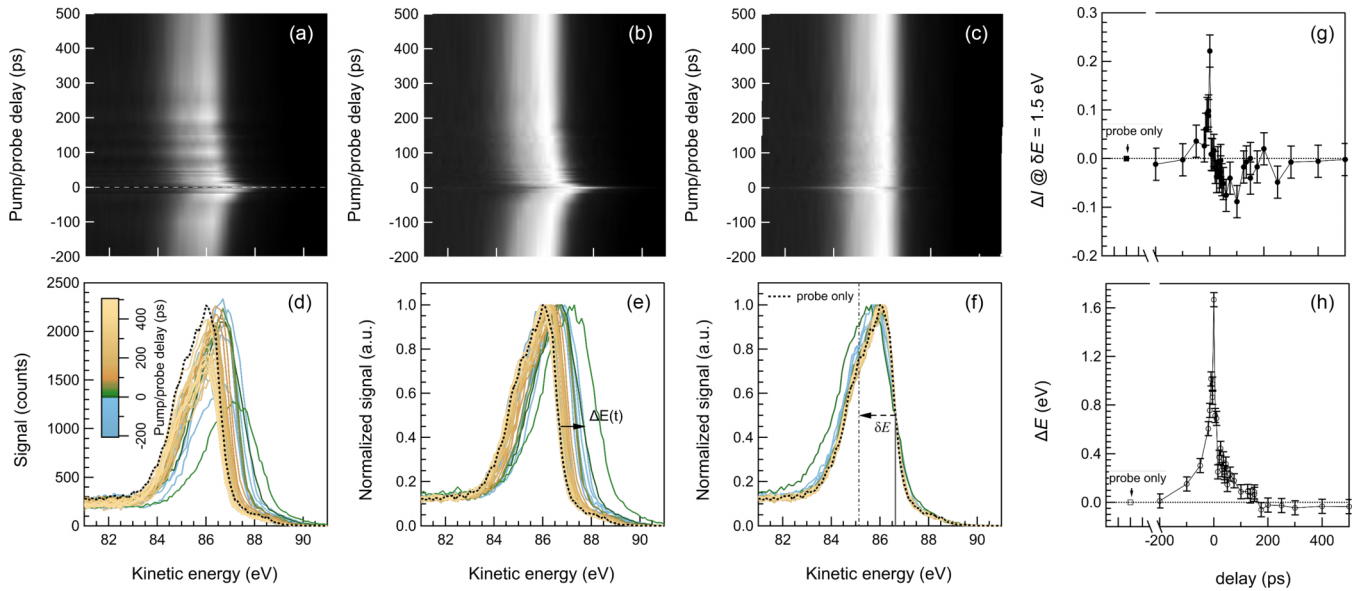
FIG. 3. Illustration of the data analysis procedure of the PES spectra recorded at $750\,\mathrm{mJ/cm^2}$ pump fluence. The cold Cu valence band, i.e., no pump irradiation, is reported in the black dotted line (probe-only PES spectrum). The upper 2D maps (a), (b), and (c) represent the temporal evolution of the Cu valence band. Negative delays refer to sample probing before the pump arrival. The lower graphs (d), (e), and (f) report all spectra recorded for this pump fluence. (a), (d) Raw data after averaging over 10 scans. (b), (e) Normalization of the signal intensity to the maximal data point. (c), (f) Spectral superimposition at the $I = 0.5$ spectral position. The last column reports the final result of the PES spectral shift, ΔE, (g) and ΔI related to the shape modifications evaluated at 1.5 ± 0.1 eV (h) referenced to the probe-only PES spectrum.

conditions, four different sets of data have been acquired, corresponding to different incident pump fluences, namely, 600, 700, 750, and 820 $\mathrm{mJ/cm^2}$. In these experimental conditions, the sample absorption is expected to be around 4%, determined by solving the Helmholtz equation using the ESTHER code. In the following, the discussion will mainly focus on the measurements performed at 750 $\mathrm{mJ/cm^2}$, while a complete qualitative interpretation is presented in Appendix A.

Figure 3 illustrates the full data set [(a) and (d)] recorded at 750 $\mathrm{mJ/cm^2}$ superimposed to the cold valence band, as well as the analysis procedure developed for this experiment [(b), (c), (e), and (f)]. This specific procedure has been applied to extract quantitative information on the modification of the Cu valence band after the pump irradiation given that space charge effects are known to also induce important alterations of the PES spectrum [7,9–11,20–25]. This is indeed evidenced in Figs. 3(a) and 3(d), where we observe, even for negative delays, that the valence band suffers important shift and broadening. In particular, the most distorted spectrum is associated with 0 ps delay. This is indeed expected since the pump-induced electron cloud will be, in this case, in closer interaction with the probe-induced one, leading to important mutual interaction. This specific zero delay measurement can also be affected by sidebands [26,27]. Furthermore, the overall PES intensity is also affected by the soft x-ray probe pulse intensity shot-to-shot fluctuations. Each spectrum is therefore first normalized to the maximum data point [Figs. 3(b) and 3(e)]. Then, a spectral shift is applied to superimpose all spectra at the kinetic energy position where the normalized signal is equal to 0.5 in the high kinetic energy part of the Cu valence band, i.e., around 86.5 eV [see Figs. 3(c) and 3(f)]. This choice is motivated by the sharp edge of the valence

band in this spectral region, allowing for a precise spectral alignment. As a result, all spectra are precisely superimposed with respect to probe-only PES spectrum.

From this data treatment, the spectral shift ΔE with respect to the probe-only PES spectrum is extracted as a function of the pump/probe delay [Fig. 3(h)]. In addition, the spectral shape modification of the Cu valence band is also characterized by quantifying the relative variation $\Delta I(\delta E)$ of the PES intensity $I(\delta E)$ at different kinetic energy positions δE [Fig. 3(f)], where $\Delta I(\delta E) = [I(\delta E) - I_{\mathrm{ref}}(\delta E)]/I_{\mathrm{ref}}(\delta E)$ and $I_{\mathrm{ref}}(\delta E)$ is the PES intensity of the probe-only spectrum. Error bars are extracted from the standard deviation of ΔE and ΔI calculated from a set of 20 probe-only PES spectra recorded consecutively.

As such, we intend to disentangle as much as possible two concomitant effects: space charge and laser heating. First, let us stress some important features in Figs. 3(g) and 3(h). At negative delays, for which no distortion or shift is expected due to laser-induced heating, ΔE and ΔI differ from zero at short time delays. These effects must therefore be due solely to space charge-induced valence band modifications. Second, ΔI, which is related to shape modifications, exhibits positive values at negative delays, while at positive ones it first decreases steeply below the zero line and slowly recovers at longer delays. This asymmetrical shape of ΔI suggests that at positive delays, in addition to space charges, another mechanism comes into play that induces an opposite distortion, presumably associated with laser heating. The spectral shift suffers a sharper decrease at positive delays, which can also be due to the two concomitant effects. These observations will be precisely investigated and discussed in the following through a detailed comparison with space charge calculations. The
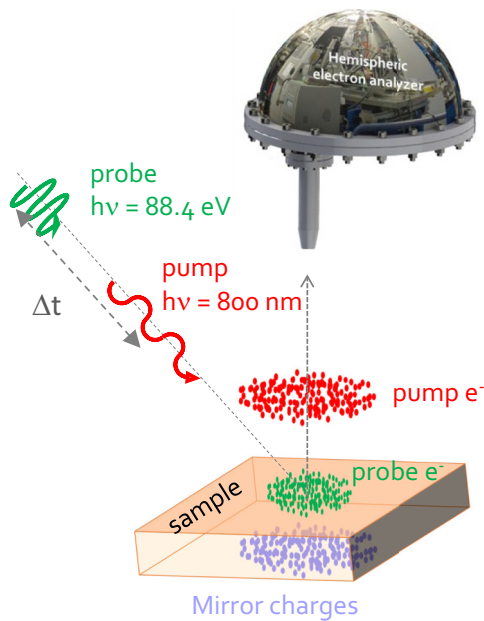
FIG. 4. Schematic representation of the pump/probe electron clouds emission.

analysis will be focused on the spectral shift, which appears to be the most reliable quantitative observable. However, the spectral modification is a reasonable qualitative observable because the valence shape is indeed expected to be modified by the increase of the sample temperature. In particular, the dip of the spin-orbit splitting of the Cu 3d valence level is in these conditions usually smeared out [28,29], justifying the focus of the above discussion in this specific spectral region of the photoelectron spectrum ($\delta E = 1.5$ eV).

III. COMPUTATIONAL DETAILS

In order to carefully interpret the experimental measurements and disentangle laser-heating and space charge effects on the Cu valence band, we have modeled the mutual interaction of the pump and probe-induced electron clouds in order to simulate the observed modifications of the PES spectrum. Indeed, from the point of view of space charges, the situation, depicted in Fig. 4, can be described as follows. The solid Cu sample is first excited by the pump pulse which generates an electron cloud leaving the sample with an initial spectral distribution mainly driven by the pump intensity. We will refer to this spectral distribution of pump electrons in the very first instants after their emission as the initial pump spectrum, as their mutual interaction can lead to significant spectral rearrangements while traveling to the detector. Indeed, the onward electrons of the cloud are accelerated by the backward part, whereas this latter is decelerated by the onward part. We will see that their initial kinetic energies are expected to range up to a few eV. While this cloud travels in the vacuum towards the detector, the probe pulse interacts with the heated sample after a given time corresponding to the pump/probe delay Δt. This results in the emission of a second electron cloud, spatially separated from the pump cloud by a given distance determined by the value of Δt. The probe-induced electron

energy distribution is, in this case, an image of the Cu valence band heated at a given temperature. However, right after their emission, these probe electrons can be influenced by the pump ones through Coulomb interaction. In addition, the probe and pump electron energy distributions are also affected by mirror charges, which tend to attract the electrons back to the sample.

According to this description, the final probe PES spectrum can be influenced by the pump cloud through complex interactions depending on several parameters including the pump/probe delay, the pump cloud electron density (i.e., laser pump pulse intensity), the initial pump spectrum, and the pump and probe spatial and angular distributions. The present study makes a step forward compared to existing works [7,23,25]. It includes a numerical calculation of the pump initial spectrum by means of the jellium-Volkov approach described in Sec. III A. This is of particular interest since this initial energy distribution, corresponding to the very first instant after the pump electron emission, cannot be measured as it is immediately distorted by its own Coulomb explosion and induced mirror charges. In addition, this study is the result of an exhaustive parametric investigation of the sensitivity of the PES induced modification to various parameters, especially the number of pump electrons and the pump and probe angular distributions. Thus, we are able to share here a comprehensive description of the space charge induced process and its consequences, which leads not only to reliable quantitative results, but, also to a benchmark study for other experiments on this topic. For that purpose, we have used the ASTRA PIC code [15] to account for space charge effects as it calculates the position and momentum evolution of the pump and probe electrons as they travel towards the detector. Their respective initial spatial and energy distribution has been initialized according to a precise parametrization as detailed in Sec. III B. This computational procedure is detailed in this section, while a comprehensive presentation of the results and their comparison to the experimental measurements are reported in Sec. IV and Appendixes B and C.

A. Calculation of the initial pump-induced electron spectrum

The initial pump spectrum is modeled using a perturbative quantum-mechanical approach named jellium-Volkov [12–14], which is less time consuming than solving the time-dependent Schrödinger equation resolution and is accurate enough for the purpose of the present work.

It is important to mention here that, according to this description, the pump-induced electron emission is due exclusively to the laser electric field component perpendicular to the sample surface. Hence an s-polarized beam should not, in principle, lead to any electron emission. Experimentally, we have confirmed this observation by comparing the s and p pump electron emissions, which significantly differ in electron number and energy. This is the reason why an s-polarized laser pulse has been used for this experiment even if the electron emission was not completely suppressed. The electron emission induced in this configuration has thus been attributed to the residual p component of the pump laser beam and the effect of the sample roughness, which is not taken into account in this model. The jellium-Volkov approach is consequently used here solely to simulate the associated pump-induced
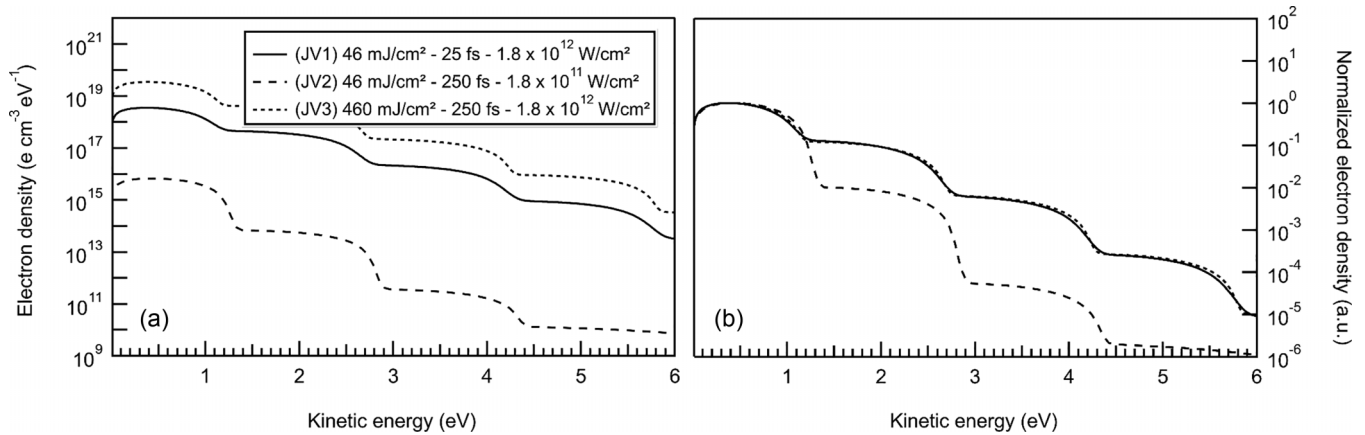
FIG. 5. (a) Initial pump spectrum using the jellium-Volkov approximation for three laser beam configurations: (1) JV1 = 46 mJ/cm^2 − 25 fs − 1.8×10^{12} W/cm^2; (2) JV2 = 46 mJ/cm^2 − 250 fs − 1.8×10^{11} W/cm^2; (3) JV3 = 460 mJ/cm^2 − 250 fs − 1.8×10^{12} W/cm^2. (b) Corresponding normalized spectra.

electron spectral shape, while the number of electrons in the cloud will be considered as a free parameter.

On this basis, the initial spectrum has been computed to simulate the electron emission induced by the pump laser pulse. A Cu sample is irradiated by a 800 nm laser pulse at 45° incidence angle. A complete calculation using the nominal 1 ps pulse duration could not be realized because of unrealistic calculation time. Instead, we have performed various calculations at different laser pulse duration and fluence in order to investigate the sensitivity of the results to these parameters.

The three investigated configurations result in the spectra reported in Fig. 5: (1) 46 mJ/cm^2 − 25 fs (1.8×10^{12} W/cm^2); (2) 46 mJ/cm^2 − 250 fs (1.8×10^{11} W/cm^2); (3) 460 mJ/cm^2 − 250 fs (1.8×10^{12} W/cm^2). In terms of shape, all three exhibit a stepwise distribution associated with the multiphoton absorption process responsible for the electron emission. Indeed, the first main component (0–1.3 eV) corresponds to the absorption of four infrared photons given the Cu work function of 4.94 eV used in the calculations. Their difference lies mainly in the electron density, which appears to be highly dependent on the laser intensity. However, here we are mainly interested in the spectral shape. Hence, from these results, one can already infer that the space charge calculations based on the pump spectrum used in configurations (1) and (3) should lead to identical results, while the configuration (2) could differ. This observation based on their respective difference is highlighted in Fig. 5(b), where the spectra have been normalized. In addition, the similarity of configurations (1) and (3) where the pulse duration is varied by one order of magnitude at constant laser intensity justify the use of a pulse duration shorter than the experimental one of 1 ps.

In the following, the space charge calculations will be presented using the initial pump spectrum of configuration (2) (denoted JV2), which corresponds to the lower investigated intensity. This choice is dictated by the experimental intensities ranging from 6×10^{11} to 8.2×10^{11} W/cm^2, which must be considered as an upper limit of the pump intensity responsible for the electron emission with the *s*-polarized laser pulse. It happens that the results obtained for configuration (1), summarized in Appendix B, lead to very similar results.

This confirms the robustness of this study, which is not highly dependent on the initial pump spectrum.

B. Space charge calculations

The space charge calculations are performed using the ASTRA PIC code [15], which computes the phase space of the electron clouds on their way to the detector. For that purpose, two clouds are defined using the cathode emission configuration of the code, which conveniently allows for the definition of pulsed particle emission of well-defined time spread and relative delay. The effect of mirror charges is included. The computational definition of the two electron clouds is initialized as follows, in close agreement with the experimental configuration, by a user-defined routine developed for the purpose of this study.

The probe-induced electrons are defined as passive particles, i.e., they will not be taken into account in ASTRA when the space charge field is calculated. In other words, we neglect the probe-induced space charge effect, which is justified by the observation that the probe-only spectrum (when the sample is not irradiated by the pump beam) was not distorted or shifted by the x-ray beam intensity. The probe electron cloud spatial and temporal distributions are an image of the probe beam intensity, [185 × 124 μm^2 (FWHM) and 25 fs Gaussian distributions, respectively]. Its spectral distribution is defined by the probe-only measured spectrum plotted in Fig. 3(d) in black dotted line. At a given temporal delay, the pump electron cloud is generated at the cathode with spatial and temporal distributions defined by the pump beam intensity [280 × 201 μm^2 (FWHM) and 1 ps Gaussian distributions, respectively]. These electrons are considered as active particles, thus participating to the space charge and mirror charge effects. Their spectral distribution follows the spectrum obtained by the jellium-Volkov model described in Sec. III A (JV2). Both clouds are defined with a sufficiently high number ($N_{part} = 10^5$) of macroparticles resulting from a trade-off between calculation time and completeness description of the spectral distributions. The calculation of the particle trajectories and momenta are performed up to 1 cm

away from the cathode plane (i.e., sample) since, after this traveling distance, the effect of space charges is negligible. The space charge effect is evaluated at various pump/probe delays spanning from -200 to 500 ps in order to mimic the experimental measurements. As such, we obtain a set of computed spectra on which the same procedure described in Sec. II B is applied for the extraction of the temporal shift ΔE and spectral distortion $\Delta I(\delta E)$ solely induced by space charges.

Using this procedure, a wide domain of parameters has been explored due to the fact that neither the pump electron number N_e nor the pump and probe angular distributions are known. We define the electron angular emissions either as Gaussian distributions of variable FWHM (θ_{FWHM}) or isotropic (θ_{iso}). For each explored situation, denoted ($\theta_{\mathrm{FWHM/iso}}^{\mathrm{IR}}$, $\theta_{\mathrm{FWHM/iso}}^{X}$) associated with the pump and probe angular distributions, respectively, N_e is optimized to fit the experimental ΔE at negative delays where no laser heating effect is expected. Each optimized ($\theta_{\mathrm{FWHM/iso}}^{\mathrm{IR}}, \theta_{\mathrm{FWHM/iso}}^{X}, N_e^{\mathrm{opt}}$) configuration is thereafter examined in order to assess the closest calculation/measurement agreement. This is achieved again by evaluating the quality of the ΔE fitting at negative delays, but also according to a second important criterion. It is based on the observation that both the space charge and the heating effects tend to enlarge the valence band [28]. However, our measurement does not evidence any significant spectral broadening. Therefore, the calculated space charge effect should also not broaden the spectral distribution of the probe electron cloud. Quantitatively, this criterion is evaluated by minimizing $\Delta I(2.25 \text{ eV})$, which would suffer important deviation in case of spectral broadening [see Figs. 12(g) and 14(g)]. Here, the 0 ps peculiar delay is excluded since, in this temporal range, important broadening is reported and indeed observed here, due to sidebands effects that are not included in this numerical modeling [26,27].

Based on this two-criteria optimization, the explored 3D ($\theta_{\mathrm{FWHM/iso}}^{\mathrm{IR}}, \theta_{\mathrm{FWHM/iso}}^{X}, N_e^{\mathrm{opt}}$) parameter space is reduced to the configuration that is closest to the experiment. The associated shift ΔE and spectral distortion $\Delta I(\delta E)$ are, in Sec. IV, qualitatively and quantitatively compared to the measurements in order to extract the effect of the pump laser heating, while the complete optimization procedures for JV1 and JV2 configurations are reported in detail in Appendix B. These calculations have been performed on the local cluster of the INSP laboratory.

C. Hydrodynamic simulations

The comparison of the measured valence band with the expected space charge effect aims at extracting the temporal dynamics of the sample irradiated by the pump laser pulse. The final discussion of this study therefore relies on the one-dimensional Lagrangian ESTHER code [16], which models the hydrodynamic evolution of the heated sample. This code includes the two-temperature model (TTM), which exploits the results from Refs. [30–32] for the different material coefficients, dependent on the electron temperature (T_e), namely the electron heat capacity (C_e), the electron thermal conductivity (k_e), and the electron-phonon coupling factor (g_{e-ph}). However, these parameters are only available for metals and data

on oxide material properties in out-of-equilibrium conditions are lacking. Hence the TTM calculation presented here will be performed with a single Cu layer and a discussion is included on the validity of this simplifed model compared to the experimental sample stack geometry. In addition, after verification, the vanadium interlayer has not been included in the present calculations given its negligible thickness (2.5 nm).

The energy deposition is implemented using the mass energy deposition module of the ESTHER code in order to model the ballistic electron energy transport expected in our case. Indeed, according to Chen and co-workers [33], below a defined value of deposited energy, the transport is driven by ballistic electrons while, above this threshold, diffusive transport dominates. This limit corresponds to the energy transported by electrons: $Q_{NT} = n_e E_F v_F$, where n_e is the electron density, v_F is the Fermi velocity, and E_F is the Fermi energy. In copper, $Q_{NT} = 1.5 \times 10^{13}$ W/cm^{-2} assuming $n_e = 8.49 \times 10^{22}$ cm^{-3}, $E_F = 7.04$ eV, and $v_F = 1.57 \times 10^{8}$ cm/s [34,35]. Given the experimental intensity used in this work lying in the range of 6 to 8.2×10^{11} W/cm^2, the present situation can be therefore safely associated with an energy transport mainly driven by ballistic electrons.

Accordingly, instead of modeling the laser-matter interaction, the pump energy is directly deposited in the sample stack assuming an exponential decay profile of characteristic lengths equal to the electron inelastic mean free path (IMFP). It is assumed here that the energy is deposited within the pulse duration of 1 ps. In Cu, the IMFP is estimated around 70 nm, while it is strongly reduced for V and Al$_2$O$_3$ down to 5 nm and 1 nm, respectively [36]. This situation has two important consequences. First, one can infer, as detailed in the following, that the copper thin layer cooling is strongly affected by the relative low thermal conductivity of the Al$_2$O$_3$ substrate ($k_{\mathrm{Al_2O_3}} = 35$ W m^{-1} K^{-1} compared to $k_{Cu} = 390$ W m^{-1} K^{-1}). Hence a particular care is dedicated here to this aspect given that the TTM calculations cannot be run with the thick oxide substrate. Second, one can suppose that the limited thermal flux through the sample bulk lowers the required laser incident fluence to reach the melting threshold at the sample surface. Hence, in this configuration, the pump laser fluence was much lower than what would have been required to achieve the same surface temperature of a thick Cu sample. This configuration is thus favorable for decoupling the pump-induced heating effect from that of space charges, since the latter are also reduced when the pump fluence is decreased.

Finally, the incident fluence is adjusted for each calculation to reach a surface temperature close to the Cu melting threshold ($T_{Cu}^m = 1358$ K). This is justified by the observation that, above the highest laser fluence used during this experimental campaign (820 mJ/cm^2), the sample surface integrity was not preserved. This was identified as the ablation threshold that could not be exceeded because the sample surface was not refreshed after each laser shot.

In the following, various numerical results are compared. The TTM is then used for three different situations, all corresponding to a single Cu layer of various thicknesses: (esth1) 5 μm; (esth2) 200 nm; (esth3) 100 nm. For all these runs, the temporal evolution of the electron and lattice temperature,
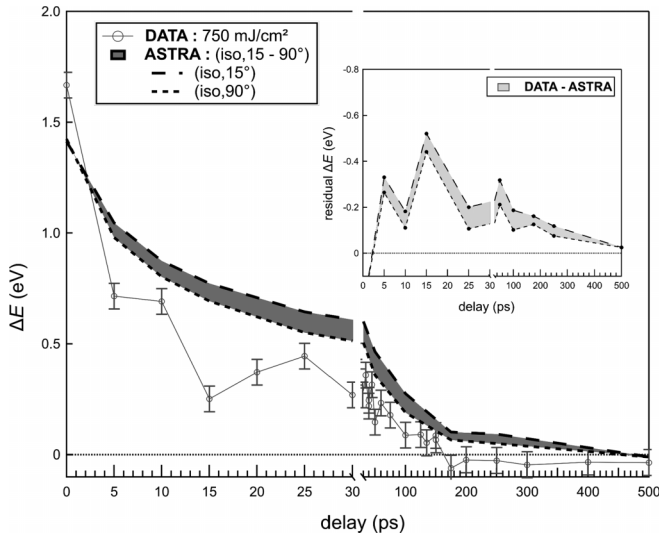
FIG. 6. Measured ($F = 750$ mJ/cm²) and calculated (ASTRA; iso, 15–90°) shift ΔE. Inset: residual shift after subtraction of the ASTRA shift to the measured one. The x axis is split in order to enhance the visibility of the short time dynamics.

denoted T_e and T_l, respectively, are extracted in order to help interpret the experimental results.

IV. RESULTS AND DISCUSSION

From this experimental and numerical twofold approach, the experimental data are examined in order to unravel the laser-heating effect on the Cu valence band, free of any space charge effect. For that purpose, the shift induced by space charges, as calculated by ASTRA, is subtracted from our measurements. In Fig. 6, the measured shift is compared to the optimal ASTRA calculations deduced from the double criteria procedure described in Sec. III B and Appendix B. This optimization of space charge calculations results in an isotropic (iso) pump electron emission and a probe electron emission described by a Gaussian angular distribution of FWHM comprised between 15 and 90°. The corresponding results

are illustrated in Fig. 6 by the dark-shaded area. Subtracting this numerical space charge contribution to the experimental measurement of the valence band shift ΔE results in the light-shaded area reported in the inset of Fig. 6. This residual shift can be therefore interpreted as an effect of the pump laser heating solely. In the following, a detailed analysis of this result is presented. Before developing our interpretation, we can extract from this result a few important comments. First, the residual ΔE is negative implying a valence band shift towards higher binding energies (i.e., lower kinetic energies). Secondly, the minimal value of about -0.5 eV is reached for a pump/probe delay of 15 ps, which is well above our experimental temporal resolution. Indeed, the latter is mainly limited by the pump pulse duration of 1 ps FWHM. Finally, the subsequent dynamics of ΔE, i.e., the valence band recovery, is characterized by long timescale in the range of a few tens of picoseconds. Hence this suggests that the sample relaxation probed in this experiment is driven by lattice changes instead of electron temperature evolution which is expected in the subpicosecond timescale [37]. Indeed, the equilibration time between lattice and electron population is usually estimated by the ratio $C_e/g_{e-\mathrm{ph}}$. For Cu, C_e is in the range of $(2-5) \times 10^5$ J m^{-3} K^{-1}, while $g_{e-\mathrm{ph}} \simeq 10^{17}$ W m^{-3} K^{-1} [30]. This rough estimation therefore already hints at timescales of the order of a few picoseconds.

In order to verify this hypothesis, our measurements are compared to ESTHER calculations performed in out-of-equilibrium conditions using the TTM. Such modeling implies a precise knowledge of material properties in this matter state, including thermal conductivities and heat capacities of the electron and atomic populations as well as the electron-phonon coupling factor. For copper, the literature is abundant [28,30,38–42], while for sapphire very few papers [43] investigate this question. Hence, given the uncertainty on the Al$_2$O$_3$ properties, we restrict our discussion to calculations on a single copper layer. The validity of this simplified approach is thereafter discussed.

In Fig. 7(a), an overview of the ESTHER calculation for a thick Cu (5 μm) sample (esth1) is illustrated in a 2D map showing the temporal evolution of the Cu temperature. For this run and the other configurations presented below, the
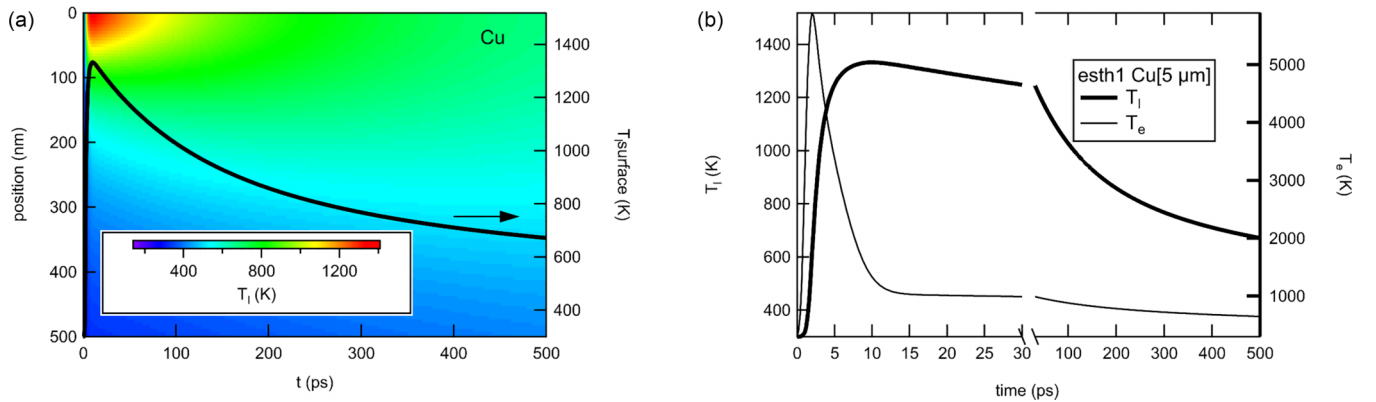

FIG. 7. Hydrodynamic ESTHER calculations. (a) 2D map of the temporal and spatial evolution of the sample lattice temperature superimposed to the dynamics of the sample surface in the case of a TTM calculation of a bulk copper sample (5 μm)-esth1. The black arrow indicates the right y axis corresponding to the temporal dynamics of the surface temperature. (b) Temporal evolution of the surface lattice (thick line) and electron (thin line) temperature for the esth1 case.
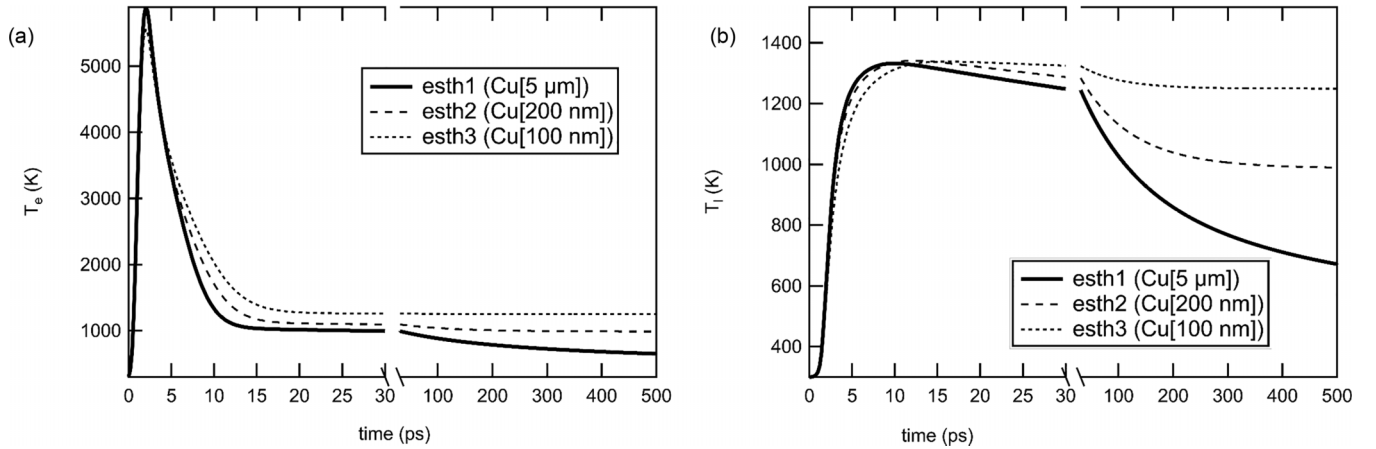
FIG. 8. Hydrodynamic ESTHER calculations. Temporal evolution of the electron (a) and lattice (b) temperature for various sample thicknesses. The corresponding sample geometries are reported in the legend.

incident energy is adjusted to reach a surface temperature close to the Cu melting threshold. This is illustrated by the top curve superimposed on the 2D map diagnosing the temperature of the first simulation mesh. Figure 7(b) compares this surface lattice temperature with the electron temperature surface dynamics. The striking result of this calculation concerns the time at which the maximal temperature is reached. This time is denoted $t_{l,e}^M$ in the following, where l stands for lattice and e for electron. Here, t_l^M approaches 10 ps, while t_e^M is reached in about 2 ps. Hence the thermal equilibrium is not established before 10 ps, which excludes the use of a single temperature calculation for this study when focusing to shorter timescales.

A direct comparison of this calculation with our experimental findings raises the question of the validity of this single Cu layer model given the very efficient energy transport into the sample bulk driven by the significant Cu thermal conductivity [see Fig. 7(a)]. Indeed, this value is in contrast with the much lower thermal conductivity of Al_2O_3, which could affect the dynamics of the sample surface. This appeals for a comparison of this calculation with the opposite case, where

the energy transport is artificially constrained by a reduced Cu thickness. The effect of the Cu thickness is explored in TTM calculations reported in Fig. 8. As expected, the energy confinement induced by a thinner Cu layer affects t_l^M but only in a small range, i.e., from 10 to 15 ps. t_e^M is reached almost simultaneously in all cases and, more importantly, the global electron temperature dynamics remains almost unchanged: after 20 ps most of the energy stored in the electron population is dissipated and the following slow T_e temporal evolution is driven by the lattice relaxation. Hence, even if these calculations are not precisely representative of the experimental stack, the overall dynamics can be directly compared to our Tr-PES results.

From these considerations, the sample dynamics extracted from our measurements is compared with ESTHER calculations in the case of the 5 μm thick copper foil (esth1). In Fig. 9, this comparison is presented for the lattice (a) and electron (b) temperatures. The dynamics of the raw residual shift ΔE, identical to data presented in Fig. 6 (inset), is clarified by presenting as well the residual shift obtained from the subtraction of DATA and ASTRA points after fitting each one
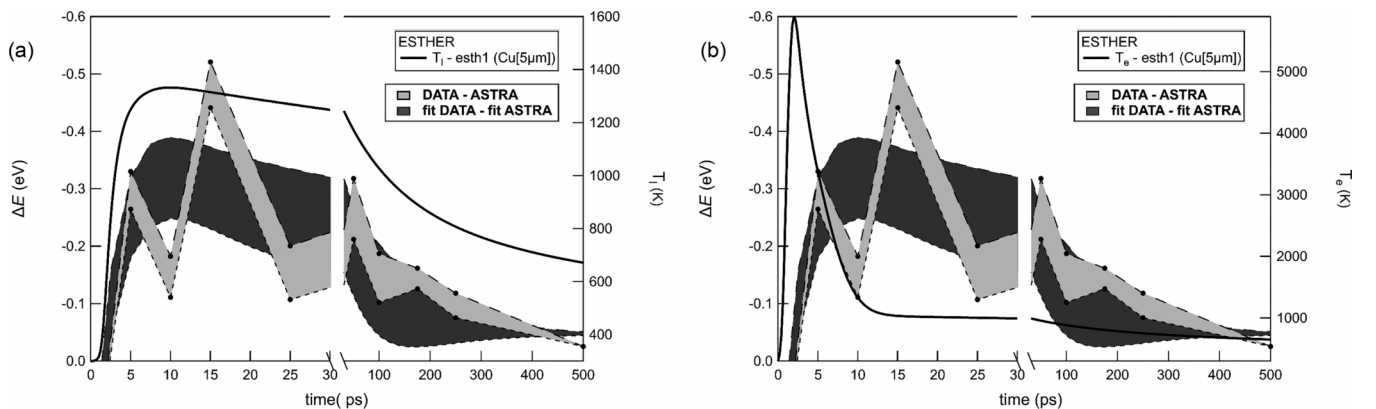

FIG. 9. Temporal evolution of the lattice (a) and electron (b) temperatures (right y axis) from ESTHER (esth1 - Cu 5 μm) compared to experimental data of the residual shift after subtraction of the ASTRA calculations (left y axis). The residual shift is reported from direct subtraction of DATA and ASTRA results (light gray area) and from subtraction of the fitted DATA and ASTRA results, including fitting 95% confidence intervals (dark gray area). For clarity reasons, the left y axis of the residual shift is inverted. The x axis is split in order to enhance the visibility of the short time dynamics.

with a biexponential function. Including the uncertainty of this prior fitting procedure with a confidence interval of 95%, this subtraction results in the dark gray area of Fig. 9 (see Appendix D for details on this procedure). As highlighted here, the global valence band dynamics induced by the sample excitation is much closer to the lattice temperature than the electron one. Indeed, the time at which the maximal absolute value of the shift is reached closely corresponds to t_l^M and not t_e^M. The same observation can be drawn when comparing the long timescale relaxation in the range of a few tens of picoseconds. Hence, assuming a linear correlation between the Cu valence shift and the lattice temperature, as suggested in Ref. [42], the probed dynamics is mostly sensitive to lattice thermal evolution as anticipated before.

These statements are hardly confirmed by current theoretical calculations since this regime of moderate temperature has not been investigated in the literature by DFT calculations. Various pertinent publications [28,38–41] are indeed focused on the out-of-equilibrium regime of solid materials, including copper, but their investigations are conducted for temperatures higher than 1 eV and the effect on the density of states is always reported as a function of the electron temperature. In addition, these calculations are usually representative of bulk materials while, in our case, the inelastic mean free path of the detected electrons ($\approx 5°$A [44]) restricts the probed volume mainly to the first atomic layer. The lower coordination of the sample surface can induce specific atomic rearrangements which can affect the electronic structure. Hence, our measurements appeal for dedicated theoretical studies in which surface effects will be taken into account. However, we believe that the present discussion sufficiently supports our interpretation to consider that our results reveal the dynamics of the sample surface lattice after an ultrafast pulsed laser pump irradiation.

V. SUMMARY

The effect of pump-induced photoelectrons in time-resolved photoelectron spectroscopy experiments in a high regime of fluence is a limiting factor as it leads to important shift and smearing of the photoelectron spectrum [6]. In principle, this effect, and especially the shift, is quantitatively predictable as it is strictly deterministic. However, this assumption implies a precise knowledge of the pump-induced electron cloud properties including charge, spectral, and geometrical characteristics. These quantities are not accessible to direct measurements since the pump electron cloud itself suffers from Coulomb explosion due to the important number of produced electrons in a reduced spatiotemporal volume. Hence the photoelectron spectrum, as measured by the electron analyzer, is strongly distorted and does not reflect its state just after exiting the sample. This study raises the possibility of bypassing this issue through a comprehensive and parametric modeling of the space charge effect in the case of a solid copper sample irradiated by an 800 nm picosecond pump laser pulse. It is based on the postulate that the measured copper valence band modification is solely due to space charges when probing at negative delays. Thereby, an optimization of the space charge calculation is achieved by exploring a wide domain of parameters associated to the pump

electron properties. These simulations, based on a jellium-Volkov [12–14] model and PIC code [15], enable a confident estimation of the shift of the valence band induced by the pump space charges and therefore we are able to extract the sample dynamics solely due to the pump-induced laser heating. Finally, the picosecond temporal change observed on the valence band, which is directly linked to a modification of the electronic density of states, is interpreted in terms of lattice temporal evolution with the help of hydrodynamic simulations including the two-temperature model. In conclusion, this work demonstrates that it is possible to disentangle space charge effects from laser-induced sample modification even at high fluence close to the metal melting threshold. It aims as well to be a benchmark study to improve our understanding of the mutual interaction of the different species emitted during time-resolved photoelectron spectroscopy experiments and, hence, open a route to tailor future experimental studies where space charges will be either controlled or reduced.

APPENDIX A: Tr-PES MEASUREMENTS AS A FUNCTION OF THE PUMP FLUENCE

In this Appendix, an exhaustive representation of the experimental results is reported in Fig. 10 including the experimental shift and valence band shape modification at various spectral values on the PES spectrum. As expected, an increasing pump fluence leads to an enhancement of both observables, which can be associated to higher sample temperature and stronger space charge effects. From this overall view of the measurements, the striking information resides in row (5) where the spectral shape modification is reported for all fluences at $\delta E = 1.5$ eV. Negative values of ΔI are solely observed at $F = 750$ mJ/cm^2. Indeed, according to reported ASTRA calculations, the space charge effect ($\Delta I > 0$) is in competition with the effect of the laser heating ($\Delta I < 0$) on the spectral shape modification. Hence one can infer that, at low fluences ($F = 600$ and 700 mJ/cm^2), the laser heating is not sufficient to induce negative ΔI values while, at higher fluences ($F = 820$ mJ/cm^2), the space charges are so strong that the negative ΔI values of the laser heating are not visible. Indeed, at this high fluence of 820 mJ/cm^2 [Fig. 10(d5)], the
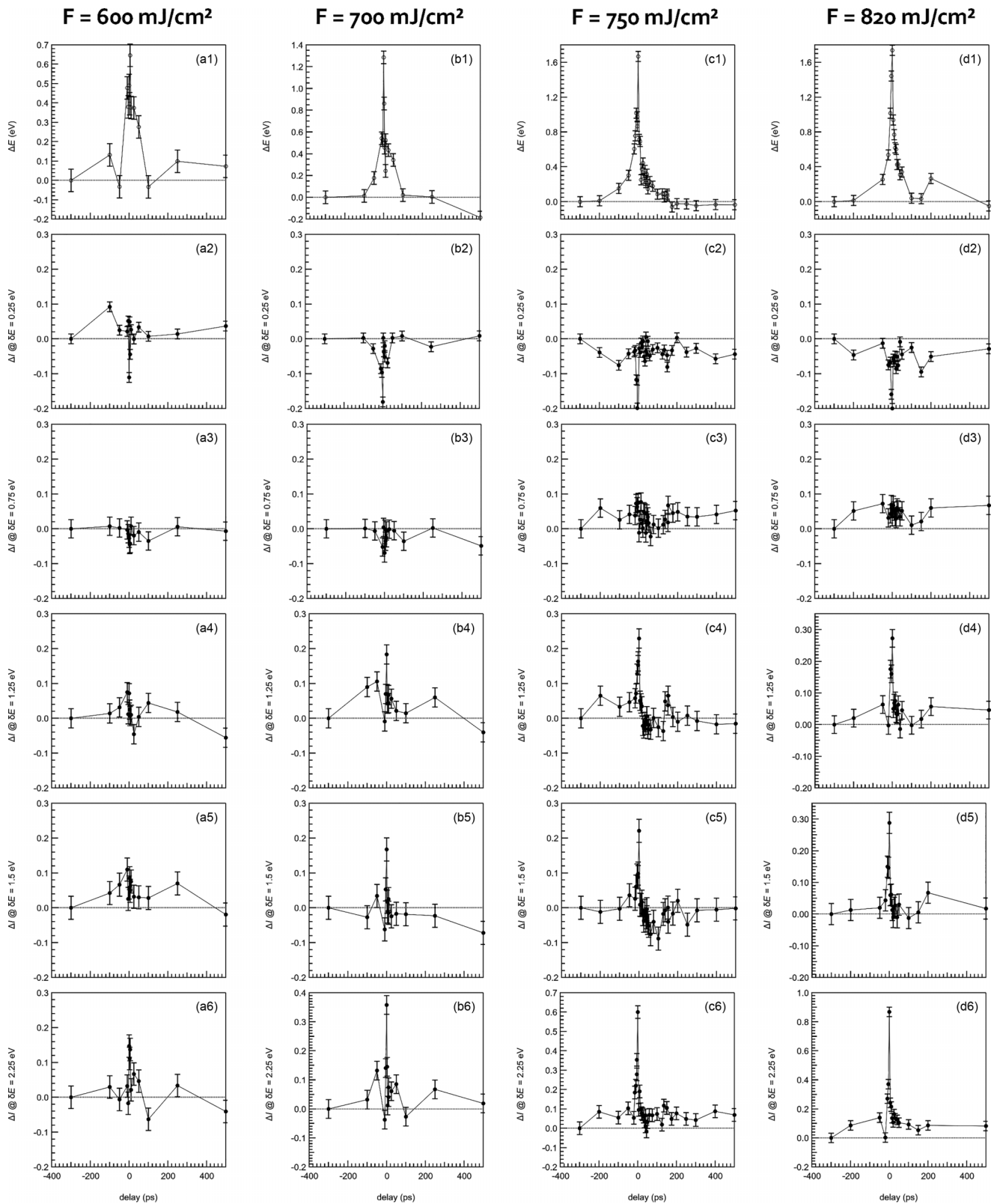
FIG. 10. Full set of experimental data for four different pump fluences: (a1)–(a6) $F = 600$ mJ/cm^2; (b1)–(b6) $F = 700$ mJ/cm^2; (c1)–(c6) $F = 750$ mJ/cm^2; (d1)–(d6) $F = 820$ mJ/cm^2. Each row labeled from 1 to 6 respectively corresponds to (1) ΔE spectral shift, (2) ΔI(0.25 eV), (3) ΔI(0.75 eV), (4) ΔI(1.25 eV), (5) ΔI(1.5 eV), and (6) ΔI(2.25 eV).
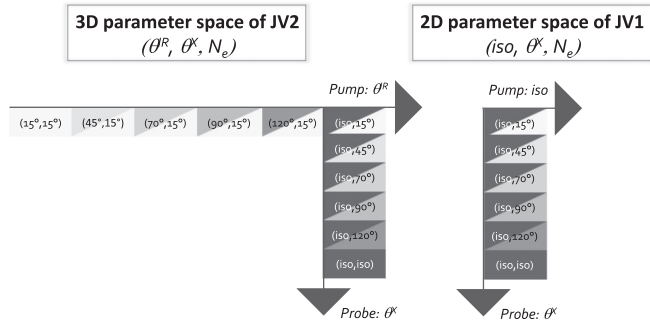
FIG. 11. Parameter spaces explored with the ASTRA space charge calculations for JV1 and JV2 configurations of the jellium-Volkov model. For each couple of pump/probe angular distributions ($\theta_{\mathrm{FWHM/iso}}^{\mathrm{IR}}$, $\theta_{\mathrm{FWHM/iso}}^{X}$), the number of pump electrons is varied in the range of about one order of magnitude in order to find the best agreement with the experimental results.

negative dip of Fig. 10(c5) is visible at positive ΔI values, confirming the above interpretation.

APPENDIX B: OPTIMIZATION PROCEDURE OF ASTRA SPACE CHARGE CALCULATIONS

In this Appendix, a detailed description of the optimization procedure of ASTRA space charge calculations is reported for JV1 and JV2 configurations of the jellium-Volkov model. These configurations are associated to two pump intensities differing in pulse duration from 25 fs to 250 fs, respectively.

As illustrated in Fig. 11, the JV2 configuration (46 mJ/cm^2 − 250 fs − 1.8 × 10^{11} W/cm^2) is investigated by exploring a 3D parameter space varying the pump ($\theta_{\mathrm{FWHM/iso}}^{\mathrm{IR}}$) and probe
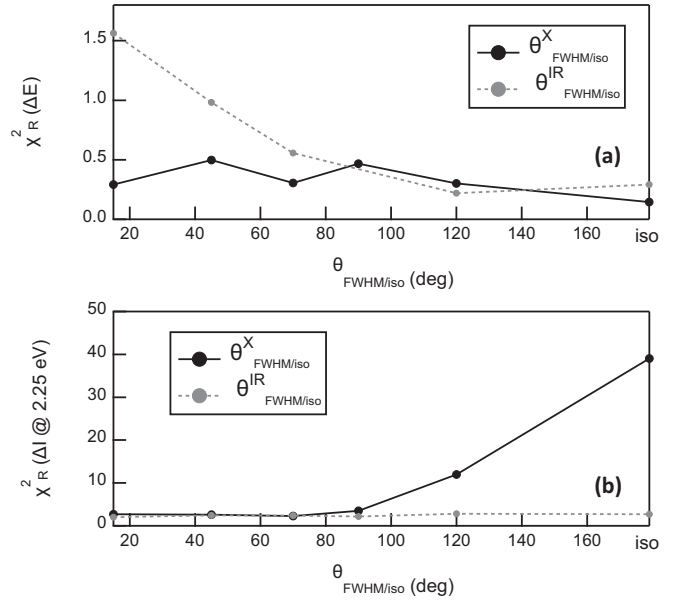

FIG. 13. Illustration of the pump and probe angular distribution optimization procedure. (a) Evolution of χ_R^2 on the spectral shift in negative delays as a function of pump and probe θ_{FWHM}. (b) Evolution of χ_R^2 on the valence band shape modification ΔI(2.25 eV) as a function of pump and probe θ_{FWHM}.

($\theta_{\mathrm{FWHM/iso}}^{X}$) angular distributions from a Gaussian shape of 15° to 120° FWHM to an isotropic emission. For each situation, the pump electron density is optimized (N_e^{opt}). In light of the JV2 results, the JV1 investigation is reduced to a 2D space where the pump angular distribution is fixed to an isotropic
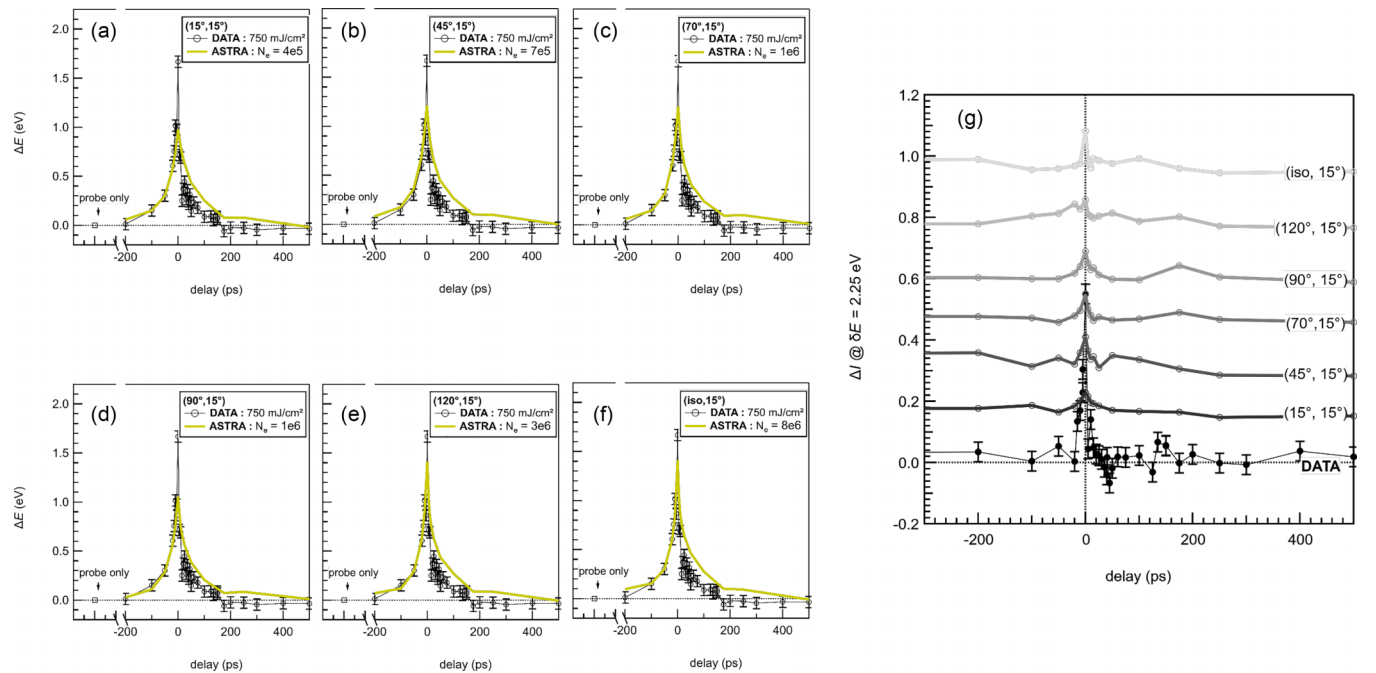

FIG. 12. Experimental and ASTRA results comparison of the spectral shift ΔE (a)–(f) and ΔI(2.25 eV) (g) for a fixed probe angular Gaussian distribution ($\theta_{\mathrm{FWHM}}^{X} = 15°$) and various pump angular emissions.
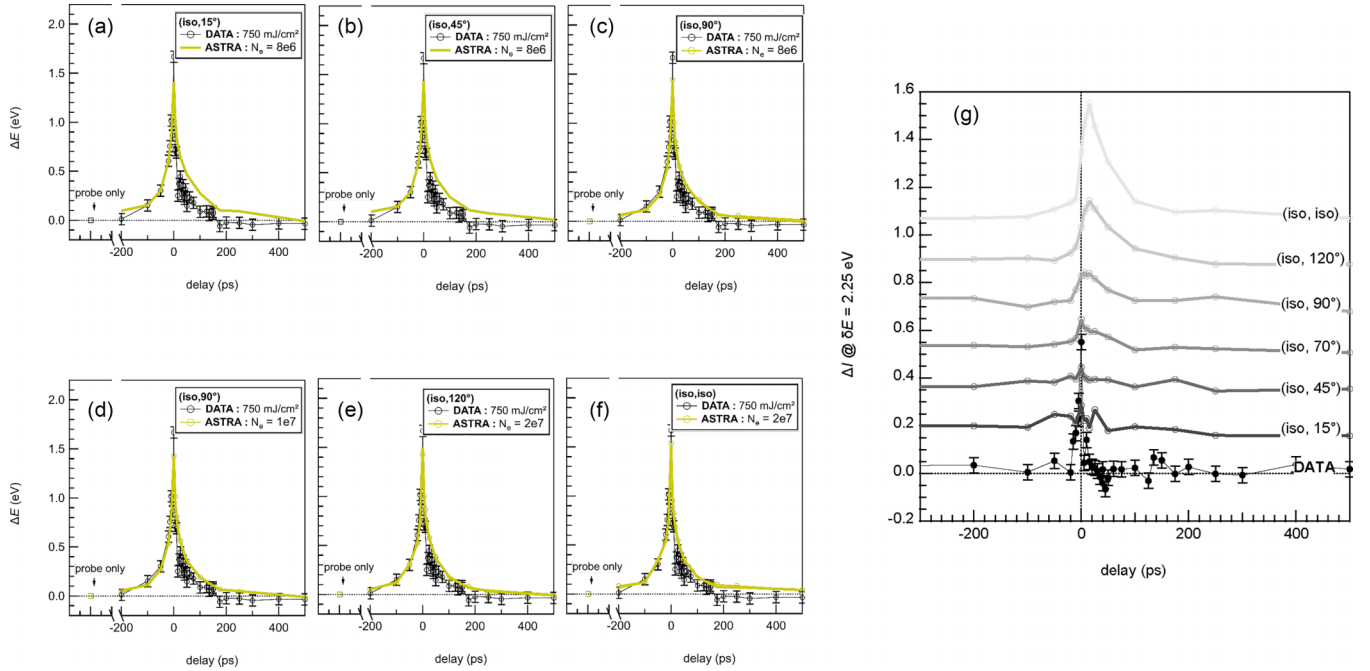
FIG. 14. Experimental and ASTRA results comparison of the spectral shift ΔE (a)–(f) and ΔI(2.25 eV) (g) for a fixed pump angular isotropic distribution and various probe angular emissions.

emission. Hence the discussion will be detailed for JV2, while the conclusions of the JV1 case will be briefly presented.

This optimization procedure of ASTRA calculations is built on the following steps.

(1) *Figures 12 and 13*. First, for a probe angular distribution fixed to $\theta^X_{\mathrm{FWHM}} = 15°$, ASTRA calculations are run for various pump angular distributions and each case is repeated for different N_e. Each associated optimal value of N_e is determined by using the least-squares method (minimization of reduced χ^2, χ^2_R) on the spectral shift ΔE in the negative delay range when comparing to experimental data. This is based on the assumption that, before the pump irradiation, spectral shifts could only be due to space charges. For these optimal values,

the ASTRA calculation is run 10 times in order to improve the result quality and extract averaged values of the spectral shift ΔE and shape modification ΔI(2.25 eV), which can now be carefully examined. From this first set of calculations, two conclusions are raised based on the evolution of χ^2_R as a function of the pump FWHM angular distribution, $\theta^{\mathrm{IR}}_{\mathrm{FWHM/iso}}$: (1) increasing the angular spread of the pump emission slightly improves $\Delta E(\Delta t < 0$ ps), while (2) ΔI(2.25 eV) values are not affected and in excellent agreement with recorded data for all cases. This is illustrated in Figs. 13(a) and 13(b) in gray dotted lines. It is therefore inferred that the pump emission is better reproduced in the isotropic configuration which is selected for the next step of the procedure.
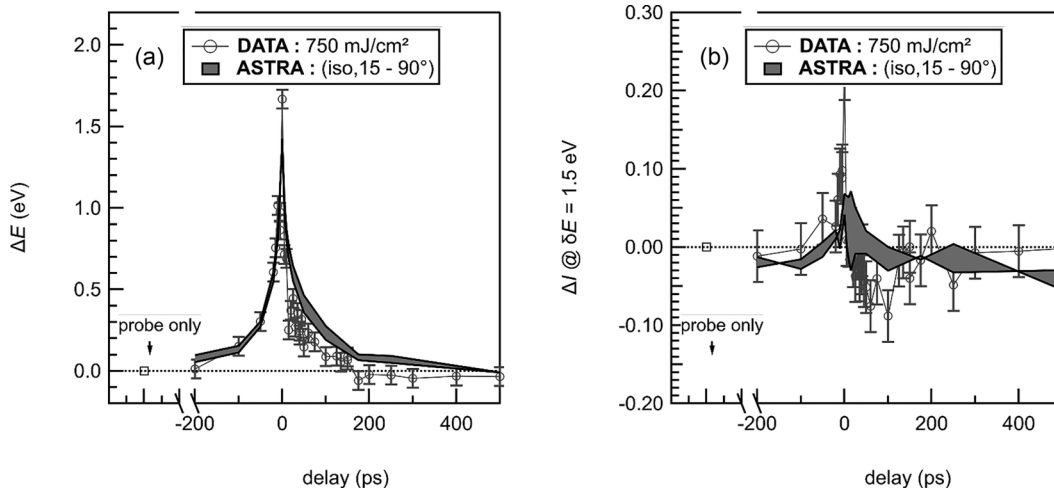

FIG. 15. Final experimental and ASTRA results comparison of the spectral shift ΔE (a) and ΔI(1.5 eV) (b) for a fixed pump angular isotropic distribution and a Gaussian probe angular emission of 15 to 90° FWHM and JV2 configuration of the jellium-Volkov model.
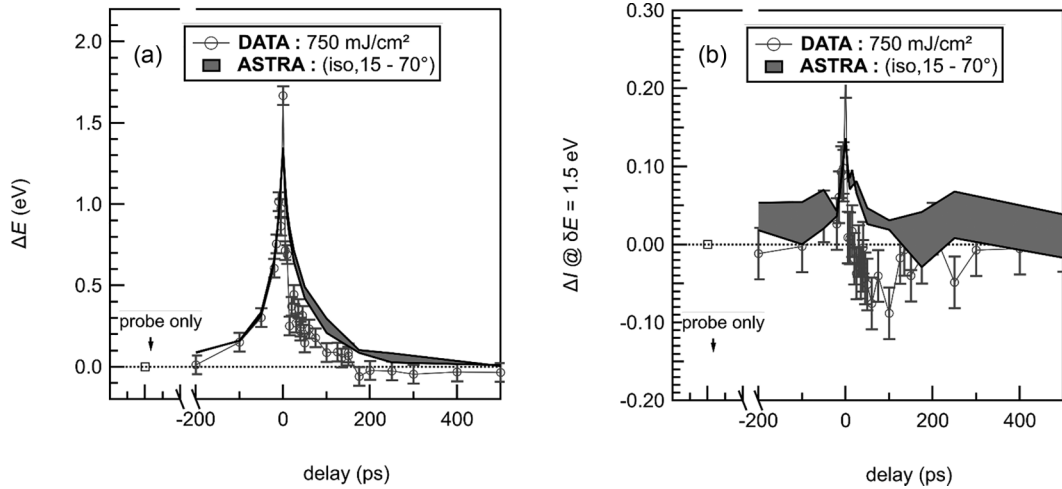
FIG. 16. Final experimental and ASTRA results comparison of the spectral shift ΔE (a) and $\Delta I(1.5\ eV)$ (b) for a fixed pump angular isotropic distribution and a Gaussian probe angular emission of 15 to $70°$ FWHM and JV1 configuration of the jellium-Volkov model.

(2) *Figure 14 and 13*. Secondly, the probe angular distribution is now varied for a fixed isotropic pump emission. Similarly, for each case, N_e is optimized. These results evidence an excellent agreement between data and ASTRA calculations of ΔE in negative delays for all explored probe angular distributions [Fig. 13(a), black line]. Instead, $\Delta I(2.25\ eV)$ is strongly affected. A reasonable agreement on this region of the spectral distortion is however preserved for $\theta_{FWHM}^{X} = 15$ to $90°$ according to χ_R^2 values reported in Fig. 13(b) (black line).

(3) *Figure 15*. On the basis of the two previous steps, an optimal region of the reduced 2D parameter space is determined. This specific case associated to the JV2 configuration corresponds to an isotropic pump emission and a Gaussian probe angular distribution of $15–90°$ FWHM. This main final result highlights a few important comments. First, the negative delay range of the spectral shift ΔE is perfectly reproduced with these ASTRA calculations, while the positive region never reaches this level of agreement [Fig. 15(a)]. This is a first hint that, in the positive delays, the measured spectral shift cannot be solely due to space charges. Consequently, the pump-induced laser heating is as well at the origin of a valence band binding energy shift. It is also worth mentioning that the space charges and the pump laser heating induce opposite effects since the measured ΔE is lower than the ASTRA calculated one. Secondly, even if much less evident, the same observation can be drawn for the spectral shape modification at $\delta E = 1.5\ eV$ [Fig. 15(b)]. Indeed, the clear negative signature of ΔI at short positive delays (<200 ps) is never reproduced by space charge calculations, indicating as well that the valence band shape is modified by the pump-induced heating. However, this argument is only invoked here as a qualitative observation given the important fluctuations on this ΔI observable both on the calculated or measured one.

As depicted in Fig. 11, the JV1 configuration is only investigated as a function of the probe angular distribution. This choice has been dictated by the insensitivity of $\Delta I(2.25\ eV)$ to the pump angular distribution and to previous upward cal-

culations, all pointing to an isotropic pump emission. The optimal results of the JV1 configuration correspond to a pump isotropic emission and a Gaussian probe angular distribution of $15–70°$ FWHM (see Fig. 16). Hence the conclusions are very similar to what is deduced from the JV2 configuration, strengthening this numerical study.

APPENDIX C: VISUALIZATION OF SPACE CHARGE EFFECT

This exhaustive study opens the opportunity to visualize and improve our understanding of the pump-induced space charge effect based on the ASTRA calculations. We propose in this Appendix to observe the temporal evolution of the probe photoelectron spectrum shift while traveling to the detector. Two cases are reported here: (A) isotropic pump and $15°$ Gaussian probe emissions and (B) isotropic pump and probe emissions. Each one is associated to two movies. First a rough representation of the pump and probe electron clouds traveling up to the position where the mutual interaction almost vanishes (≈ 3 mm) (see Supplemental Material [44] movies mvA.1.mp4 and mvB.1.mp4). Then, a second movie focuses on the earlier stage when the probe electron cloud is crossing and overtaking the pump one (≈ 50 μm) (see Supplemental Material [44] movies mvA.2.mp4 and mvB.2.mp4). These movies are extracted for a pump/probe delay of 50 ps. The spatial positions of the probe and pump electrons are reported on the 3D plot in blue and red dots, respectively. Correspondingly, the probe electron spectrum is compared to the reference one (without pump electrons).

From these representations, one can raise a few observations. First, the effect of the pump-induced space charges almost vanishes after a very short distance from the emission point (sample). This is due both to the very rapid Coulomb explosion of the pump electron cloud and the very different pump and probe electron kinetic energies (a few eV and a few tens of eV, respectively) which lead to a quick separation of the two clouds. Secondly, in both cases, the positive shift of the probe electron kinetic energies is the result of two
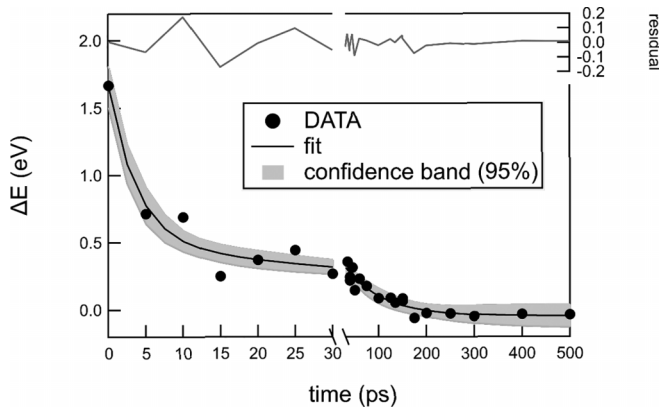
FIG. 17. Experimental measured valence band shift compared to the result of fitting analysis using a biexponential function. The confidence interval of 95% is reported in the gray area and the residuals are added in the upper curve.

different phases. The probe cloud is first decelerated while being emitted up to a point where it overtakes the pump cloud, which then pushes ahead the probe electrons. The shift is therefore alternatively negative and then positive. The two situations (A) and (B) reported here differ by the resulting shift ΔE, which is lower in the second case and by the respectively much more important shape induced modification ΔI(2.25 eV). Both are due to a much less uniform pump-induced effect related to the probe isotropic emission. Indeed, while traveling in the transverse dimension, the probe electrons experience a weaker pump-induced effect which differs from the ones that are emitted in the normal direction. This induces both a broadening of the probe electron spectra and a less efficient kinetic energy shift.

APPENDIX D: FITTING PROCEDURE FOR EXTRACTION OF THE RESIDUAL SHIFT DUE TO LASER-HEATING EFFECT

In this Appendix, the fitting results used to extract the residual shift of Fig. 9 are detailed.
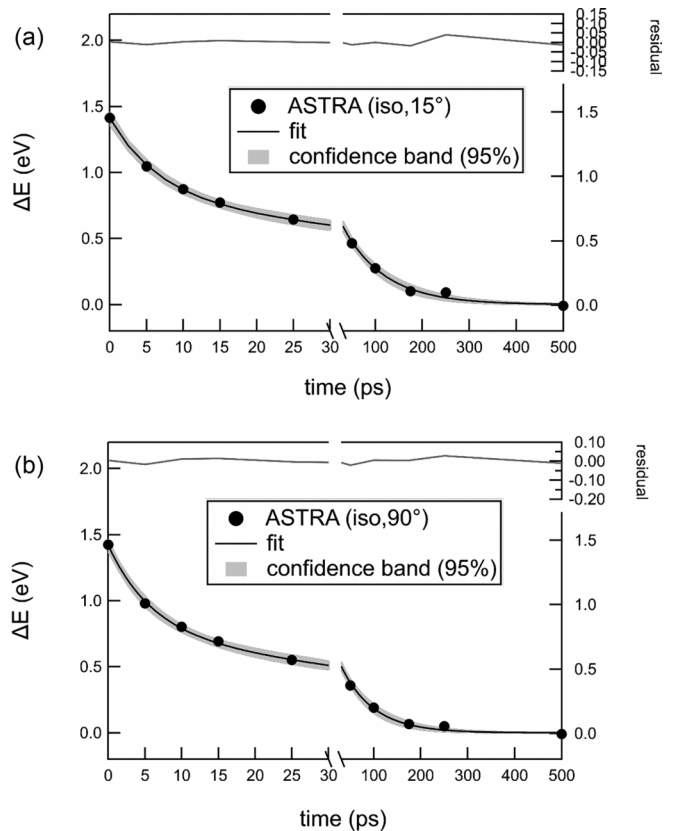

FIG. 18. ASTRA calculated valence band shift compared to the result of fitting analysis using a biexponential function. The confidence interval of 95% is reported in the gray area and the residuals are added in the upper curve: (a) ASTRA run for (iso, 15°) configuration and (b) ASTRA run for (iso, 90°).

(1) First, the measured shift of the valence band (DATA) is fitted using a biexponential function. The uncertainty of this fitting procedure is taken into account using confidence bands in a confidence interval of 95%. Both the optimal fit and corresponding band are illustrated in Fig. 17.

(2) Then the same analysis is applied to ASTRA results of the two limits of the optimization procedure (iso, 15°) and (iso, 90°). Both are reported in Fig. 18.

[1] M. S. Schuurman and V. Blanchet, Phys. Chem. Chem. Phys. **24**, 20012 (2022).

[2] P. M. Kraus, M. Zürch, S. K. Cushing, D. M. Neumark, and S. R. Leone, Nat. Rev. Chem. **2**, 82 (2018).

[3] G. Lantz, B. Mansart, D. Grieger, D. Boschetto, N. Nilforoushan, E. Papalazarou, N. Moisan, L. Perfetti, V. L. R. Jacques, D. Le Bolloc'h, C. Laulhé, S. Ravy, J.-P. Rueff, T. E. Glover, M. P. Hertlein, Z. Hussain, S. Song, M. Chollet, M. Fabrizio, and M. Marsi, Nat. Commun. **8**, 13917 (2017).

[4] Y. Kim and J. Lee, npj Comput. Mater. **6**, 132 (2020).

[5] S. Beaulieu, M. Schüler, J. Schusser, S. Dong, T. Pincelli, J. Maklar, A. Neef, F. Reinert, M. Wolf, L. Rettig, J. Minár, and R. Ernstorfer, npj Quantum Mater. **6**, 93 (2021).

[6] G. Schönhense, D. Kutnyakhov, F. Pressacco, M. Heber, N. Wind, S. Y. Agustsson, S. Babenkov, D. Vasilyev, O. Fedchenko, S. Chernov, L. Rettig, B. Schönhense, L. Wenthaus, G. Brenner, S. Dziarzhytski, S. Palutke, S. K. Mahatha, N. Schirmel, H. Redlin, B. Manschwetus *et al.*, Rev. Sci. Instrum. **92**, 053703 (2021).

[7] L.-P. Oloff, K. Hanff, A. Stange, G. Rohde, F. Diekmann, M. Bauer, and K. Rossnagel, J. Appl. Phys. **119**, 225106 (2016).

[8] L.-P. Oloff, M. Oura, K. Rossnagel, A. Chainani, M. Matsunami, R. Eguchi, T. Kiss, Y. Nakatani, T. Yamaguchi, J. Miyawaki, M. Taguchi, K. Yamagami, T. Togashi, T. Katayama, K. Ogawa, M. Yabashi, and T. Ishikawa, New J. Phys. **16**, 123045 (2014).

[9] S. Hellmann, C. Sohrt, M. Beye, T. Rohwer, F. Sorgenfrei, M. Marczynski-Bühlow, M. Kalläne, H. Redlin, F. Hennies, M. Bauer, A. Föhlisch, L. Kipp, W. Wurth, and K. Rossnagel, New J. Phys. **14**, 013062 (2012).

[10] G. Schiwietz, D. Kuehn, A. Foehlisch, K. Holldack, T. Kachel, and N. Pontius, J. Electron Spectrosc. Relat. Phenom. **220**, 40 (2017).

[11] D. Leuenberger, H. Yanagisawa, S. Roth, J. Osterwalder, and M. Hengsberger, Phys. Rev. B **84**, 125107 (2011).

[12] N. Fedorov, G. Geoffroy, G. Duchateau, L. Stolcova, J. Proska, F. Novotny, M. Domonkos, H. Jouin, P. Martin, and M. Raynaud, J. Phys.: Condens. Matter **28**, 315301 (2016).

[13] H. Jouin, M. Raynaud, G. Duchateau, G. Geoffroy, A. Sadou, and P. Martin, Phys. Rev. B **89**, 195136 (2014).

[14] M. N. Faraggi, M. S. Gravielle, and D. M. Mitnik, Phys. Rev. A **76**, 012903 (2007).

[15] D. Klaus Floettmann, Astra software download and manuals, http://tesla.desy.de/~meykopff/.

[16] J. P. Colombier, P. Combis, F. Bonneau, R. Le Harzic, and E. Audouard, Phys. Rev. B **71**, 165406 (2005).

[17] N. Fedorov, S. Beaulieu, A. Belsky, V. Blanchet, R. Bouillaud, M. D. A. Villa, A. Filippov, C. Fourment, J. Gaudin, R. E. Grisenti, E. Lamour, A. Levy, S. Mace, Y. Mairesse, P. Martin, P. Martinez, P. Noe, I. Papagiannouli, M. Patanen, S. Petit *et al.*, Rev. Sci. Instrum. **91**, 105104 (2020).

[18] M. Aeschlimann, C. A. Schmuttenmaer, H. E. Elsayed-Ali, R. J. D. Miller, J. Cao, Y. Gao, and D. A. Mantell, J. Chem. Phys. **102**, 8606 (1995).

[19] F. Catoire, A. Ferré, O. Hort, A. Dubrouil, L. Quintard, D. Descamps, S. Petit, F. Burgy, E. Mével, Y. Mairesse, and E. Constant, Phys. Rev. A **94**, 063401 (2016).

[20] G. Schiwietz, D. Kuehn, A. Foehlisch, K. Holldack, T. Kachel, and N. Pontius, J. Synchrotron Radiat. **23**, 1158 (2016).

[21] X. Zhou, B. Wannberg, W. Yang, V. Brouet, Z. Sun, J. Douglas, D. Dessau, Z. Hussain, and Z. Shen, J. Electron Spectrosc. Relat. Phenom. **142**, 27 (2005).

[22] A. Pietzsch, A. Foehlisch, M. Beye, M. Deppe, F. Hennies, M. Nagasono, E. Suljoti, W. Wurth, C. Gahl, K. Doebrich, and A. Melnikov, New J. Phys. **10**, 033004 (2008).

[23] R. Al-Obaidi, M. Wilke, M. Borgwardt, J. Metje, A. Moguilevski, N. Engel, D. Tolksdorf, A. Raheem, T. Kampen, S. Maehl, I. Y. Kiyan, and E. F. Aziz, New J. Phys. **17**, 093016 (2015).

[24] S. Hellmann, K. Rossnagel, M. Marczynski-Bühlow, and L. Kipp, Phys. Rev. B **79**, 035402 (2009).

[25] M. Dell'Angela, T. Anniyev, M. Beye, R. Coffee, A. Föhlisch, J. Gladh, S. Kaya, T. Katayama, O. Krupin, A. Nilsson, D. Nordlund, W. F. Schlotter, J. A. Sellberg, F. Sorgenfrei, J. J.

Turner, H. Östrom, H. Ogasawara, M. Wolf, and W. Wurth, Struct. Dyn. **2**, 025101 (2015).

[26] L. Miaja-Avila, C. Lei, M. Aeschlimann, J. L. Gland, M. M. Murnane, H. C. Kapteyn, and G. Saathoff, Phys. Rev. Lett. **97**, 113604 (2006).

[27] G. Saathoff, L. Miaja-Avila, M. Aeschlimann, M. M. Murnane, and H. C. Kapteyn, Phys. Rev. A **77**, 022903 (2008).

[28] N. Jourdain, V. Recoules, L. Lecherbourg, P. Renaudin, and F. Dorchies, Phys. Rev. B **101**, 125127 (2020).

[29] B. I. Cho, K. Engelhorn, A. A. Correa, T. Ogitsu, C. P. Weber, H. J. Lee, J. Feng, P. A. Ni, Y. Ping, A. J. Nelson, D. Prendergast, R. W. Lee, R. W. Falcone, and P. A. Heimann, Phys. Rev. Lett. **106**, 167601 (2011).

[30] Z. Lin, L. V. Zhigilei, and V. Celli, Phys. Rev. B **77**, 075133 (2008).

[31] C. Wu, D. A. Thomas, Z. Lin, and L. V. Zhigilei, Appl. Phys. A **104**, 781 (2011).

[32] R. Li, O. A. Ashour, J. Chen, H. E. Elsayed-Ali, and P. M. Rentzepis, J. Appl. Phys. **121**, 055102 (2017).

[33] Z. Chen, V. Sametoglu, Y. Y. Tsui, T. Ao, and A. Ng, Phys. Rev. Lett. **108**, 165001 (2012).

[34] N. W. Ashcroft and N. D. Mermin, *Solid State Physics* (Harcourt College Publishers, New York, 1976).

[35] A. Grolleau, F. Dorchies, N. Jourdain, K. Ta Phuoc, J. Gautier, B. Mahieu, P. Renaudin, V. Recoules, P. Martinez, and L. Lecherbourg, Phys. Rev. Lett. **127**, 275901 (2021).

[36] J. Hohlfeld, S.-S. Wellershoff, J. Güdde, U. Conrad, V. Jähnke, and E. Matthias, Chem. Phys. **251**, 237 (2000).

[37] B. Rethfeld, A. Kaiser, M. Vicanek, and G. Simon, Phys. Rev. B **65**, 214303 (2002).

[38] N. Jourdain, L. Lecherbourg, V. Recoules, P. Renaudin, and F. Dorchies, Phys. Rev. B **97**, 075148 (2018).

[39] E. Bevillon, J. P. Colombier, V. Recoules, and R. Stoian, Phys. Rev. B **89**, 115117 (2014).

[40] B. I. Cho, T. Ogitsu, K. Engelhorn, A. A. Correa, Y. Ping, J. W. Lee, L. J. Bae, D. Prendergast, R. W. Falcone, and P. A. Heimann, Sci. Rep. **6**, 18843 (2016).

[41] G. M. Petrov and A. Davidson, Plasma Phys. Controlled Fusion **63**, 125011 (2021).

[42] J.-W. Lee, M. Kim, G. Kang, S. M. Vinko, L. Bae, M. S. Cho, H.-K. Chung, M. Kim, S. Kwon, G. Lee, C. H. Nam, S. H. Park, J. H. Sohn, S. H. Yang, U. Zastrau, and B. I. Cho, Phys. Rev. Lett. **127**, 175003 (2021).

[43] M. Toulemonde, C. Dufour, A. Meftah, and E. Paumier, Nucl. Instrum. Methods Phys. Res. Sect. B **166-167**, 903 (2000).

[44] See Supplemental Material at http://link.aps.org/supplemental/10.1103/PhysRevB.109.174311 for movies mvA.1.mp4, mvB.1.mp4, mvA.2.mp4, and mvB.2.mp4.